Implementing SPAM into STMAS: A net sensitivity improvement in high-resolution NMR of quadrupolar nuclei

J.P. Amoureux [a],*, L. Delevoye [a], G. Fink [b], F. Taulelle [b], A. Flambard [a], L. Montagne [a]

[a] *LCPS, CNRS-8012, ENSCL-USTL, Fr-59652 Villeneuve d'Ascq, France*
[b] *UVSQ, Versailles, France*

Abstract

Gan and Kwak recently introduced two new tools for high-resolution 2D NMR methods applied to quadrupolar nuclei: double-quantum filtering in STMAS (DQF–STMAS) and the soft-pulse added mixing (SPAM) idea. Double-quantum filtering suppresses all undesired signals in the STMAS method with limited loss in sensitivity. With SPAM, all pathways are added constructively after the second hard-pulse instead of using a single pathway as previously. Here, the sensitivity, advantages and drawbacks of DQF–STMAS are compared to 3QMAS. Additionally, SPAM can be included into DQF–STMAS method, resulting in a net sensitivity gain with respect to 3QMAS of ca. 10–15.
© 2005 Elsevier Inc. All rights reserved.

Keywords: Quadrupolar nuclei; MQMAS; STMAS; SPAM

1. Introduction

Nuclei with spin $S > 1/2$, undergo a quadrupolar interaction. The size of this interaction can be described by the quadrupole coupling constant $C_Q = e^2qQ$, which is equal to the product of the quadrupole moment eQ of a nucleus and the electric field gradient at the nucleus eq. For half-integer spins, the first-order quadrupolar effect on the satellite transition (ST) frequencies ($m - 1 \leftrightarrow m$, $m \neq 1/2$) is of the order of C_Q. However, the central transition (CT: $-1/2 \leftrightarrow 1/2$) is only affected to the second-order. Since this contribution is typically 10^2–10^3 times smaller than C_Q, the central transition yields a narrower and more intense spectrum, which is the subject of most studies on half-integer spin quadrupolar nuclei. Most studies of quadrupolar nuclei in the last two decades utilized the line-narrowing effect of magic-angle spinning (MAS) [1]. MAS eliminates the first-order broadening completely and reduces the quadrupolar contribution to the CT line width by a factor of approximately 3. Recently, it has been demonstrated by Frydman and Harwood [2] that the CT line narrowing can be obtained without changing the orientation of the spinning axis, as long as the motion of the rotation axis in space is replaced by changing the coherence state of the observed spins. This experiment, referred to as multiple quantum MAS (MQMAS), is a 2D method, which correlates the phase evolutions of the MQ and single quantum coherences and allows for observation of a purely isotropic echo. Very recently, another technique referred to as satellite transition MAS (STMAS) has been proposed [3]. This technique provides isotropic spectra of half-integer quadrupolar nuclei by correlating the evolution of single quantum inner-STs ($\pm 3/2$, $\pm 1/2$) in t_1 with that of the CT during t_2. Since ST coherences can be excited and converted to the CT very efficiently by strong RF pulses, the STMAS experiment provides an interesting alternative to MQMAS.

For all crystallite orientations, both methods refocus the second-order quadrupole dephasings along a unique axis with equation: $t_2 = R(S) \, t_1$ [4]. This refocusing allows obtaining 2D frequency spectra from which the first indirect dimension becomes, after shearing, an isotropic dimension (δ_{iso}), and the second dimension (δ_2) is the classical MAS one. The comparison of all MQMAS (3QMAS, 5QMAS, ...) and STMAS results has been facilitated recently by the introduction of a unified ppm representation for all methods [5]. In this representation, that we will use in the following, resonances are always located at the same places in the 2D spectra, which means that they always have the same isotropic (δ_{iso}) and anisotropic (δ_2) projections.

Since their initial proposals, numerous developments have been proposed for MQMAS and STMAS. They were first concerned with getting pure absorption 2D spectra, and the elaborated sequences fit in two categories of methods, which are amplitude-modulated (AM) or phase-modulated (PM). The first category of sequences generally includes a *z*-filter part [6–9], whereas the second one is of full-echo type [10–13].

In STMAS (and MQMAS), the most frequently used sequences are composed of three pulses: two hard-pulses (HP$_1$ for the creation of inner-STs and then, after t_1, HP$_2$ for their conversion) with RF-field amplitudes in the 50–200 kHz range, followed by one soft-pulse (SP) of amplitude in the 5–20 kHz range. Hard-pulses are able to affect all coherences of the density matrix, whereas soft-pulses can only modify those concerning the central-transition. However, NMR is an insensitive spectroscopy, which often requires numerous accumulations, especially for 2D high-resolution methods (MQMAS and STMAS) applied to quadrupolar nuclei in solids. In order to enhance the sensitivity, very recently, an improvement, christened SPAM, that concerns the ensemble HP$_2$–SP has been proposed [14]. Up to now, in all STMAS sequences, a single coherence quantum level is selected in between HP$_2$ and SP: $0Q$ in *z*-filter and $+1Q$ in full-echo experiments. The idea proposed by Gan and Kwak [14] is to use in a constructive way all quantum levels in between HP$_2$ and SP. One of the two methods proposed, called soft-pulse added mixing (SPAM), aliases completely all the coherence transfer pathways. Recently, we verified theoretically and experimentally, that the use of SPAM pulses (ensemble HP$_2$–SP) in MQMAS, allows doubling the echo-signal, and that its introduction into high-resolution 2D methods allows gaining a factor of 2.8–3 for the S/N ratio with respect to the S/N ratio that can be obtained with the original *z*-filter MQMAS experiment [15].

This contribution analyzes if the intrinsically larger (with respect to 3QMAS) efficiency that can be obtained with STMAS method, can be combined with the large S/N gain that can be obtained by using the SPAM concept. First, we summarize the advantages and limitations that are intrinsically related to the STMAS principle. Then, we compare STMAS to 3QMAS relative sensitivities. Finally, we include SPAM into STMAS, and establish theoretically and experimentally, the S/N gain that can be obtained on test samples as well as industrial compounds.

2. The DQF–STMAS method

The STMAS method refocuses second-order quadrupole dephasings acting on inner-STs during the evolution time t_1 with those acting on CT during the observation time t_2. This simple principle results in several practical details related to the fact that STs are (i) on the same coherence level as CT, and (ii) are simultaneously submitted to first- and second-order quadrupole interactions.

2.1. Elimination of unwanted transfers

An undesired feature of 2D STMAS spectra is the presence of one uninformative autocorrelation CT–CT ridge and, if $S > 3/2$, of resonances arising from magnetizations that are situated during t_1 on outer-STs $\{(\pm m, \pm(m - 1))$ with $m > 3/2\}$ [3,12]. The CT–CT narrow ridge overlaps with the targeted signal especially in case of weak quadrupole interactions or broad resonances, such as those encountered in disordered or amorphous samples. Resonances related to outer-STs obscure the spectra and complicate their interpretation. Although these two types of signals are unwanted, it is impossible to remove them from the spectrum by phase-cycling [16] because they both result from the evolution of single-quantum coherences during t_1. Three different methods have been proposed concerning the CT–CT ridge: (i) this signal can be reduced by pre-saturation [17], or suppressed either (ii) by using a half rotor-period t_1 increment [12] or (iii) by acquiring an additional rotor-off-synchronized dataset [18]. These approaches suffer from either incomplete CT–CT suppression or loss of a factor of 2 for the S/N ratio. Moreover, these methods do not solve the problem related to outer-STs if $S > 3/2$.

The most recently proposed method removes all unwanted signals by using a double-quantum filter (DQF) [19]. In this approach, an additional CT selective π pulse is employed during the t_1 period. In the framework of a perfectly selective π pulse, inner-STs transform as double-quantum coherences, CT only changes by two quantum levels ($1Q \leftrightarrow -1Q$), and outer-STs remain unaffected on one-quantum levels. A classical phase cycling procedure thus allows an easy selection on the $\pm 2Q$ levels of the "good" ST–CT signal (Fig. 2). DQF has already found another application in sol-

id-state NMR of quadrupolar nuclei, in filtering double-quantum signal originating either from dipolar coupling or from the quadrupolar multilevel systems [20]. The introduction of this selective π pulse does not change a lot the sensitivity with respect to the original STMAS method. Indeed, it has been shown that it decreases by only ca. 20–25% the full-echo signal [19,21], and that it
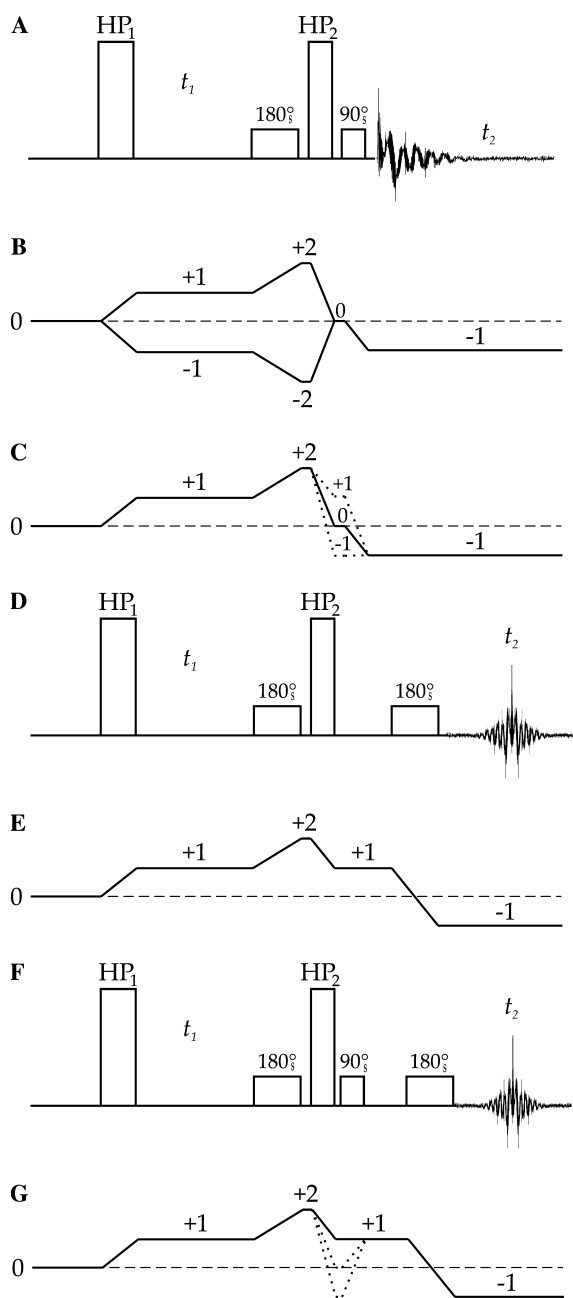

Fig. 2. ^{27}Al STMAS spectra of $AlPO_4$ berlinite recorded with the original (left) and DQF (right) versions. $B_o = 11.7$T, $v_0 = 130.2$ MHz, $v_R = 10$ kHz. Only one aluminum species exists in berlinite. The CT-CT ridge disappears with the DQF version. Experimental time: 5 min, RF-field: 108 and 15 kHz for hard-pulses and soft-pulses, respectively.

may even slightly (10%) increase the signal intensity with respect to the z-filter sequence [19]. Moreover, the fact that all unwanted signals have been canceled allows a very simple optimization of all experimental parameters directly on the spectrum. The double-quantum filter principle is very efficient and very robust, and will always be used in the following. It has been proposed in two different versions [19], the DQF–STMAS and DQ–STMAS experiments, which only differ by the fact the additional selective π pulse is at the end (DQF–STMAS) or at the beginning (DQ–STMAS) of the t_1 period. A comparison of the two methods (S/N ratio, sensitivity to magic-angle misset and spinning speed instability, isotropic resolution, and spectral-width,...) has not yet been done. We have thus chosen to use the DQF–STMAS method, which is very similar to the original STMAS method.

2.2. Pulse-length optimization

We just mentioned that introducing an accurate selective π pulse during t_1, cancels all unwanted signals. With real samples, due to off-resonance irradiation and second-order quadrupole interactions, this pulse cannot be a perfectly selective π pulse for all species simultaneously. There are therefore small transfers to the DQ levels of magnetizations that were previously on CT and outer-STs coherences on $1Q$ levels. However, these coherences are not refocused at the mixing pulse due to the rotor-synchronization, and they do not give rise to unwanted signals [19]. The effect of this imperfect π pulse is thus to slightly decrease the targeted ST–CT signal. Therefore weak unwanted signals may originate either from incomplete phase-cycling, or spin-diffusion on $0Q$ level for the CT–CT signal observed with the z-filter method. In any case, a weak (but not too small to irradiate the second-order quadrupole frequency spread) RF amplitude (5–20 kHz) is recommended for the selective pulses.

Fig. 1. DQF–STMAS. (A) Pulse sequence for z-filter, SPAM$_E$, SPAM$_{AE}$, and SPAM$_{E/AE}$. Coherence transfer pathways corresponding to: (B) z-filter and (C) SPAM$_E$ ($S > 3/2$) or SPAM$_{AE}$ ($S = 3/2$). Pulse sequence (D) and coherence transfer pathway (E) for full-echo ($S > 3/2$) or full-antiecho ($S = 3/2$) methods. SPAM$_{FE}$ ($S > 3/2$) or SPAM$_{FAE}$ ($S = 3/2$) pulse sequence (F) and coherence transfer pathway (G).
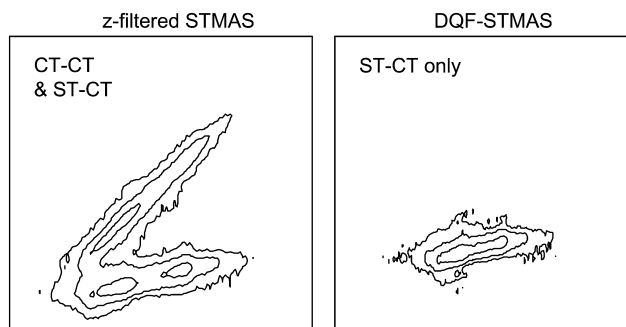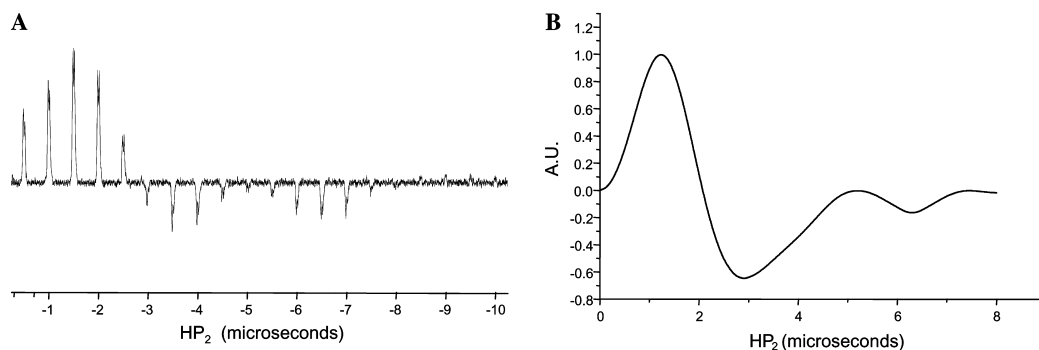
Fig. 3. Optimization of HP_2 length in ^{27}Al DQF–STMAS of $AlPO_4$ berlinite. $B_0 = 11.7$ T, $v_0 = 130.2$ MHz, RF-field = 200 kHz, $v_R = 10$ kHz. (A) Experimental spectra; (B) theoretical curve.

Optimization of other RF amplitudes and pulse-lengths is as easy as in MQMAS. Amplitudes of the two hard-pulses (HP_1 and HP_2) must be as large as possible, and that of the last selective pulse (after HP_2) must be of the same order (5–20 kHz) as the previous selective π pulse. All corresponding pulse-lengths can easily be optimized by maximizing for the first $t_1 = T_R = 1/v_R$ step either the ST–CT echo on the FID, or its Fourier transform. In all STMAS experiments, it is very important to start the HP_2 optimization with a small pulse-length. Indeed, according to the pulse-length value, the final ST–CT signal changes in sign (Fig. 3), and starting from a too long pulse-length may thus lead to the second maximum which is less efficient, and submitted to a much weaker S/N SPAM enhancement (see & IV) than the first one.

2.3. Adjustment of the magic angle

Any type of STMAS experiment correlates the second-order quadrupole dephasings (ϕ_{Q2}) acting on STs during t_1 with those acting on CT during t_2. However, and contrary to MQ coherences in MQMAS, STs are also submitted to first-order quadrupole interactions. These interactions imply that related large first-order dephasings (ϕ_{Q1}) must be perfectly cancelled. To do so, two things must very accurately be fulfilled: the rotor-axis must always be exactly adjusted at the magic angle ($\theta_M = 54.736°$), and the evolution time t_1 must be perfectly rotor-synchronized.

Actually, the rotor axis is never exactly set at the magic angle ($\theta = \theta_M + \Delta\theta$). For powder samples observed in STMAS-based experiments, the total isotropic line-width related to $\Delta\theta$ and corresponding to both inner-STs is equal to

$$\Delta\delta_{iso}(\text{ppm}) \approx AC_Q\Delta\theta/v_0, \tag{1}$$

when given in 'normalized' ppm scaling [5]. v_0 is the Larmor frequency, $\Delta\theta$ must be given in degrees, and $A = 13067$, 10453, 9334, and 8712 for $S = 3/2$, 5/2, 7/2, and 9/2, respectively. As an example, $\Delta\delta_{iso} =$

3.66 ppm, if $\Delta\theta = 0.005°$, $C_Q = 7$ MHz, $S = 5/2$, and $v_0 = 100$ MHz. The broadening effect of a magic angle miss-adjustment increases proportionally to the quadrupole interaction, and to the reciprocal of the Larmor frequency.

Recently, an STMAS method that is self-compensated for angle missets (SCAM–STMAS) has been proposed [22]. This method introduces an additional hard-pulse in the middle of the evolution period, that transfers coherence between symmetrical satellite transitions. As a result, the SCAM–STMAS experiment yields superior isotropic resolution than STMAS, without the need of a too accurate θ adjustment. However, the S/N ratio is decreased by a factor of ca. 3 and the isotropic spectral-width by a factor 2 (this is due to the additional π pulse, as experimentally evidenced in [20]).

Usually, experimental setting of the magic angle is achieved by maximizing the number and amplitude of ST spinning sidebands from solids with small quadrupole interactions. This accuracy is insufficient for STMAS. In each FID of an STMAS experiment, the ST–CT echo amplitude is very sensitive to the exact value of the magic angle. Maximizing the ST–CT echo amplitude of the first FID ($t_1 = 1/v_R$) is thus a much more precise method for angle calibration [18]. However, a rapid acquisition of 2D DQF–STMAS spectra on a model compound is often required to precisely set the magic angle. When changing the sample with automatic ejection/insertion of the rotors, changes of the spinning angle axis remain very small, especially if a small amount of bearing gas is applied to "soften the landing" of the rotor in the stator [21]. In any case, the very small broadening due to remaining miss-adjustment of the magic angle is not visible on 2D spectra of distributed samples, such as zeolites, glasses, or amorphous compounds. The calibration of the magic angle, whether on a model compound or on the material of interest itself, should be performed at the spinning speed that will be employed in the final 2D experiment, as the magic angle setting is sensitive to

the spinning speed [21]. A good STMAS probe head requires an improved adjustment rod to allow very fine setting of the magic angle.

2.4. Spinning speed

To cancel ϕ_{Q1}, the evolution time t_1 must be rotor-synchronized to pick the top of ST rotational echoes. Due to the fact that ϕ_{Q1} is much larger than ϕ_{Q2}, this rotor-synchronization must be perfect, and the definition of t_1 time must take into account the two hard-pulse lengths. On the opposite, these pulse-lengths are most of the time not taken into account in MQMAS where only ϕ_{Q2} intervenes. Another important consequence of this perfect rotor-synchronization is that the spinning speed must be perfectly stable. However, it is not really easy to obtain such a good stability, especially when compressors are starting to increase the air pressure in the tanks [21]. When the spinning speed is too much fluctuating (several Hz),

Fig. 4. ^{27}Al isotropic projection of AlPO$_4$ berlinite DQF–STMAS spectra recorded with different spinning speeds: $v_R = 8000$ (A), 8003 (B), 8006 (C), 8010 (D), and 8015 (E) Hz. The fluctuations about these previous values are ca. ± 2 Hz. The value $v_R = 8000$ Hz was always introduced in the pulse program.

significant broadenings are observed in the δ_{iso} dimension, resulting in a considerable sensitivity decrease. This broadening effect can be observed in (Fig. 4) displaying the isotropic projections of AlPO$_4$ berlinite, which presents only one aluminum species, recorded with different spinning speeds about the value $v_R = 8$ kHz that was introduced in the pulse program. Even for a small difference of 3 Hz, there is an amplitude decrease of 15% with respect to the best experimental case (compare Figs. 4A and B). Moreover, even when the spinning speed is kept relatively stable (ca. within 1–2 Hz), it is common to observe a t_1 noise fluctuation on the isotropic projection (Fig. 4A) [18,22]. This t_1 noise, which is not visible on the anisotropic projection, still remains a limitation of all STMAS methods. One way to improve the speed stability is by using several tanks after the air compressor, several evenly spaced marks on the rotor, and a good speed controller. By doing so, it has been shown that the spinning rate can indeed be controlled within ± 0.1 Hz [23,24].
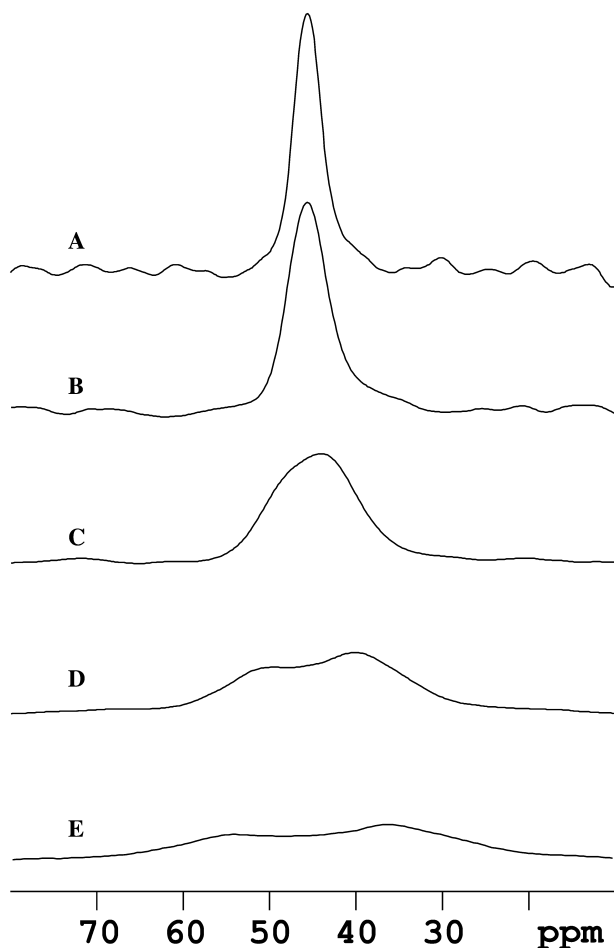
3. DQF–STMAS sensitivity

3.1. Pulse-sequence and pathways

In AM (z-filter) high-resolution 2D spectra of half-integer spin quadrupolar nuclei, the final signal mainly results from the echo pathway. Indeed, the anti-echo signal of AM experiments cancels after only a few t_1 slices (especially for spin values with a large $R(S)$ factor, and/or species submitted to large C_Q values and/or distributions of surroundings) and the corresponding 2D absorptive contribution is weak. In AM methods, the magnetization issuing from the anti-echo pathway is thus mainly used to minimize the dispersive parts that come from the echo pathway. In DQF–STMAS, the signal thus results from the following pathways for AM and PM experiments:

$$AM : 0Q \rightarrow -1Q(t_1 - t_\pi) \rightarrow -2Q(t_\pi) \rightarrow 0Q \rightarrow -1Q(t_2)$$
$$\text{if } S = 3/2, \tag{2}$$

$$0Q \rightarrow +1Q(t_1 - t_\pi) \rightarrow +2Q(t_\pi) \rightarrow 0Q \rightarrow -1Q(t_2)$$
$$\text{if } S > 3/2, \tag{3}$$

$$PM : 0Q \rightarrow +1Q(t_1 - t_\pi) \rightarrow +2Q(t_\pi) \rightarrow +1Q(\tau + Rt_1)$$
$$\rightarrow -1Q(\tau + t_2) \quad \text{if } S = 3/2, \tag{4}$$

$$0Q \rightarrow +1Q(t_1 - t_\pi) \rightarrow +2Q(t_\pi) \rightarrow +1Q(\tau)$$
$$\rightarrow -1Q(\tau + Rt_1 + t_2) \text{ if } S > 3/2. \tag{5}$$

Transfers related to hard-pulses or soft-pulses are indicated by ⇢ or →, respectively. The first selective pulse length (t_π) must be incorporated in the definition of the evolution time t_1. Two other PM pathways can also be used for $S = 3/2$. These pathways describe a full echo signal, which means that a delay τ shorter than that corresponding to Eq. (4), which describes a full anti-echo signal, can be used. The first one, $0Q \rightarrow -1Q(t_1 - t_\pi) \rightarrow -2Q(t_\pi) \rightarrow +1Q(\tau) \rightarrow -1Q(\tau + Rt_1 + t_2)$, requires a three-quantum level jump for HP$_2$, and is thus much less efficient than the one described in Eq. (4) that requires only a one-quantum level jump. The second one is a split-t_1: $0Q \rightarrow +1Q(9t_1/17 - t_\pi) \rightarrow +2Q(t_\pi) \rightarrow +1Q(\tau + 8t_1/17) \rightarrow -1Q(\tau + t_2)$ [12]. It has the same efficiency as that described by Eq. (4), but with an isotropic spectral-width decreased by a factor of 9/17.

To quantify the maximum efficiency that can be obtained with these methods, we have carried out a systematical numerical analysis of the optimal transfer conditions. For four RF-field amplitudes (50, 100, 150, and 200 kHz) for the hard-pulses, and as a function of the C_Q value, we have maximized the powder-averaged final CT value by varying systematically the hard-pulse lengths (HP$_1$ and HP$_2$) as well as the amplitude and lengths of the soft-pulses. We have adopted a MAS speed just sufficient to eliminate sidebands in the observation dimension (δ_2), irradiations were always done on-resonance, and the Larmor frequency was fixed to

$v_0 = 105$ MHz. It must be noted that the results of our calculations are similar to those recently published [25], for which a quasi-static rotor was however assumed during the pulses.

Optimal HP$_1$ lengths were always found identical for all STMAS-based sequences: AM or PM, with or without double quantum filtering, and with or without the SPAM concept (see & IV). They only depend on the spin value S, the C_Q value, and the hard-pulse RF-field amplitude. The optimal soft-pulse just before HP$_2$ is always very close to 180_s°. For AM and PM experiments, the optimum last soft-pulse is always equal to 90_s° and 180_s°, respectively.

CT values represented in (Figs. 5, 6, and 11) are normalized with respect to the signal that can be observed in 1D experiments after a 90_s° soft-pulse. When using a PM sequence, a full echo (Eq. (5)) or full anti-echo (Eq. (4)) is normally observed if the delay τ is sufficient. This doubles the signal, but also increases simultaneously the noise by a factor of $\sqrt{2}$. To compare directly signal to noise (S/N) ratios obtained in AM and PM experiments, CT values represented for PM experiments (Figs. 5B, D, 6B, D, and 11) were multiplied by $\sqrt{2}$. However, a complete comparison of AM and PM S/N ratios requires also taking into account the supplementary attenuation $\exp(-\tau/T'_{2ST} - \tau/T'_{2CT})$, which occurs on PM values due to homogeneous dipolar interactions. Practically, a proper S/N comparison requires the use of spectra recorded with identical experimental conditions:
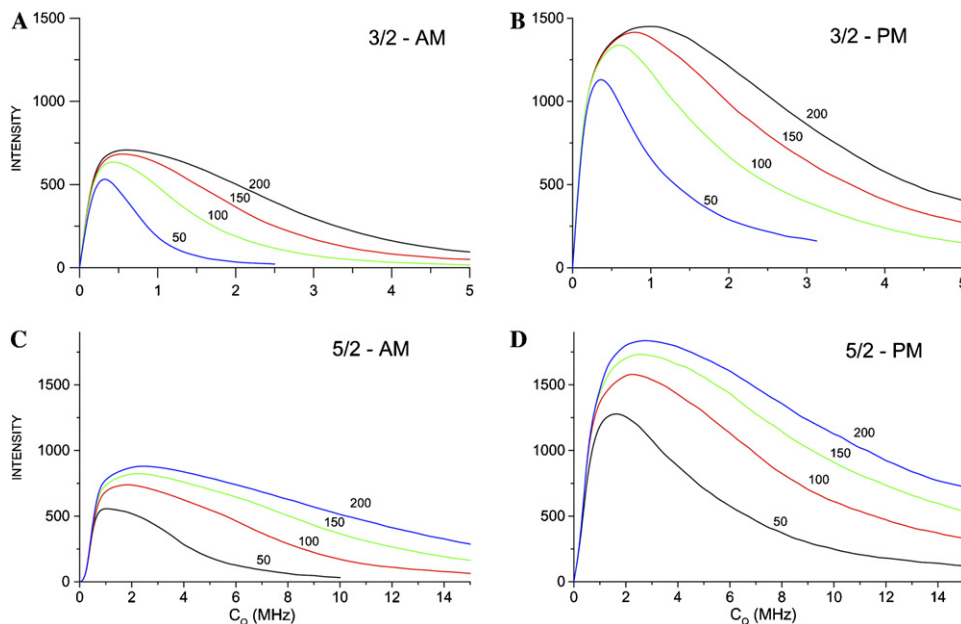

Fig. 5. DQF–STMAS: efficiency of the echo pathway in AM (*z*-filter). (A) $S = 3/2$ ($0 \rightarrow -1 \rightarrow -2 \rightarrow 0 \rightarrow -1$), (C) $S = 5/2$ ($0 \rightarrow +1 \rightarrow +2 \rightarrow 0 \rightarrow -1$) or PM (B) $S = 3/2$, (D) $S = 5/2$ ($0 \rightarrow +1 \rightarrow +2 \rightarrow +1 \rightarrow -1$) experiments, as a function of C_Q (A,B: 0–5 MHz; C,D 0–15 MHz). B$_1$(HP) = 50, 100, 150, 200 kHz. $\eta_Q = 0$. $v_0 = 105$ MHz. (A,B) $v_R = 10$ kHz ($C_Q < 3$ MHz), $v_R = 15$ kHz ($C_Q > 3$ MHz); B$_1$(SP) = 5 kHz ($C_Q < 2$ MHz), 10 kHz ($2 < C_Q < 3$ MHz), 20 kHz ($C_Q > 3$ MHz). (C and D) $v_R = 10$ kHz ($C_Q < 9$ MHz), 15 kHz ($9 < C_Q < 12$ MHz), 20 kHz ($C_Q > 12$ MHz); B$_1$(SP) = 5 kHz ($C_Q < 7$ MHz), 10 kHz ($7 < C_Q < 9$ MHz), 20 kHz ($C_Q > 9$ MHz).
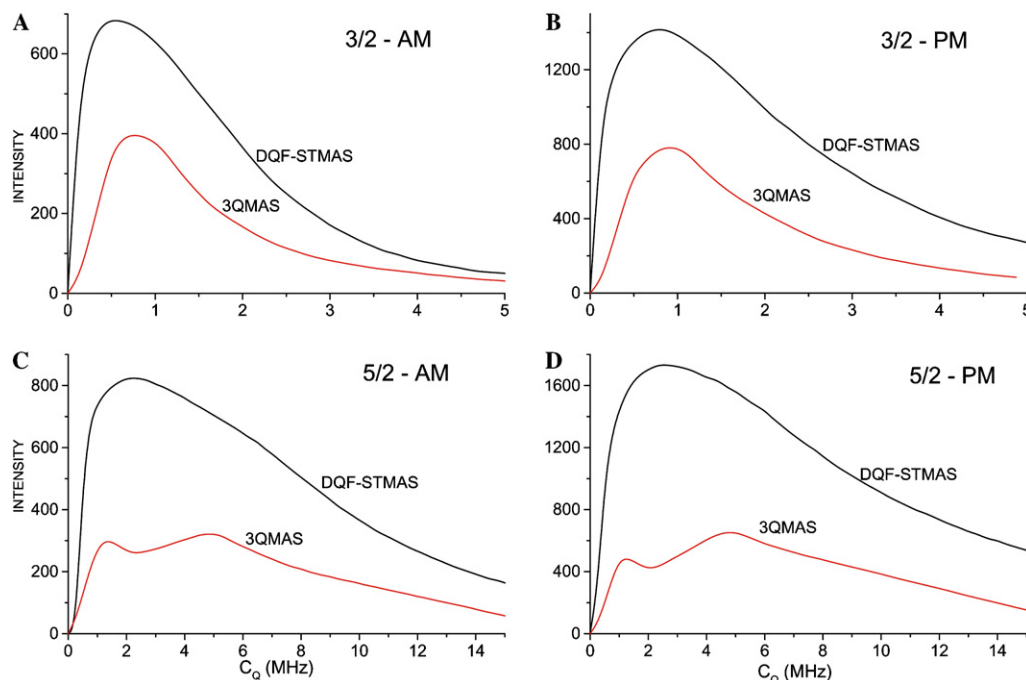
Fig. 6. Efficiency of the echo pathway in z-filter (AM) type of experiments (A): $S = 3/2$ DQF–STMAS ($0 \rightarrow -1 \rightarrow -2 \rightarrow 0 \rightarrow -1$), 3QMAS ($0 \rightarrow -3 \rightarrow 0 \rightarrow -1$), (C): $S = 5/2$ DQF–STMAS ($0 \rightarrow +1 \rightarrow +2 \rightarrow 0 \rightarrow -1$), 3QMAS ($0 \rightarrow +3 \rightarrow 0 \rightarrow -1$), or (PM) full-antiecho (B: $S = 3/2$) or full-echo (D: $S = 5/2$) type of experiments: DQF–STMAS ($0 \rightarrow +1 \rightarrow +2 \rightarrow +1 \rightarrow -1$) and 3QMAS ($0 \rightarrow +3 \rightarrow +1 \rightarrow -1$), as a function of C_Q(A,B: 0–5 MHz; C,D: 0–15 MHz). B_1(HP) = 150 kHz. All other specifications as in Fig. 5.

spinning speed, RF-fields, recycling delay, and total acquisition time.

3.2. Sensitivity

It must be noted here that due to the very large first-order dephasings (ϕ_{Q1}) involved in this experiment, pulse-lengths must be taken into account experimentally and computationally. Sensitivities that can be obtained for AM and PM experiments are displayed respectively in Figs. 5A and B for $S = 3/2$ and Figs. 5C and D for $S = 5/2$. S/N ratio observed in DQF–STMAS is approximately doubled in PM experiments with respect to AM experiments. The reduction in sensitivity for weak quadrupole interactions ($C_Q < 300$ kHz) is related to the fact that the two SP pulses are then no more CT-selective. This phenomenon is completely different to that obtained in MQMAS where the much smoother beginning of the curves is related to the fact that transfers are in-between observable and unobservable parts of the density matrix (Fig. 6). Because only one 3Q coherence participates during t_1 to the signal, calculated sensitivity of 3QMAS is approximately half ($S = 3/2$) or one third ($S = 5/2$) that of DQF–STMAS where both symmetrical inner-STs are used (Fig. 6). One important conclusion that can be deduced from Figs. 5 and 6, is that the best sensitivity with original (not using the SPAM concept) 3QMAS and DQF–STMAS methods is observed with PM (full-echo or full-antiecho) DQF–STMAS experiments if irreversible T_2' effects can be neglected.

Figs. 5 and 6 represent the powder averaged CT coherence, multiplied by $\sqrt{2}$ in PM experiments, that can be observed at the time origin: $t_1 \approx t_2 \approx 0$ in 3QMAS and $t_1 = T_R$ and $t_2 = R(S) T_R$ in DQF–STMAS. It must nevertheless be reminded that in the previous calculations only first- and second-order quadrupole interactions were introduced, that irradiations were always assumed on-resonance, and that losses related to irreversible T_2' effects were neglected. However, in order to fully compare sensitivities related to 3QMAS and DQF–STMAS experiments, several other interactions must be introduced. These interactions may decrease either the efficiency of the transfers or the S/N ratio of the 2D spectra by broadening their isotropic projections. Moreover a complete comparison of the methods requires taking into account two experimental specifications related to the spinning speed: the isotropic spectral widths, and the minimum evolution time to avoid truncation of the signal along the t_1 dimension.

3.3. Other interactions

It has been shown that MQMAS sensitivity decreases when CSA becomes important [26]. In Fig. 7A, we have represented the sensitivity that can be obtained in 3QMAS and DQF–STMAS on a spin $S = 5/2$, versus the CSA amplitude for a fixed spinning speed. It can be observed that the relative loss of sensitivity versus CSA is much more critical in 3QMAS than in DQF–STMAS experiments, especially for weak RF-fields.
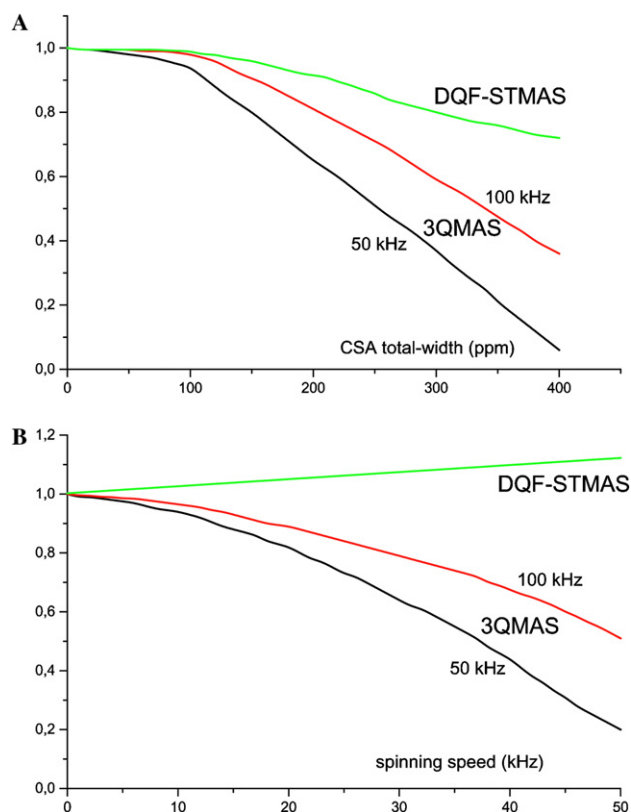
Fig. 7. $S = 5/2$: relative efficiency that can be observed: (B) versus v_R (no CSA), and (A) versus the total CSA line-width ($\sigma_{33} - \sigma_{11}$) with $v_R = 10$ kHz. $\eta_\sigma = 0$, aligned quadrupolar and CSA tensors, $v_0 = 130.3$ MHz, $C_Q = 4.09$ MHz, $\eta_Q = 0.35$. 3QMAS with RF (HP) = 50 kHz, and 100 kHz. In DQF–STMAS, both RF-fields give nearly the same results.

The fact that STMAS-based methods are less sensitive to CSA, is a large advantage when trying to analyze nuclei with large atomic number, especially at high magnetic fields.

Isotropic projections may be broadened by: (i) third-order quadrupole interactions in STMAS [27], or by cross terms of the quadrupole interaction: either (ii) with CSA in STMAS [28], or with dipolar interaction with (iii) a spin 1/2 in STMAS [21] or (iv) with another quadrupolar nucleus in MQMAS and STMAS [13]. These line broadenings decrease the required minimum number of t_1 steps, at the expense of the S/N ratio and the isotropic resolution. Happily, broadenings related to interactions (i, iii, and iv) decrease when increasing the magnetic field because they are inversely proportional to the Larmor frequency [21]. Actually, the main broadening in all STMAS-based methods arise from short T'_{2ST} values for ST coherences. Indeed, it has recently been shown that during t_1 ST coherences in STMAS, which are submitted to first-order quadrupole interactions, are much more sensitive to molecular motions that MQ coherences in MQMAS, which are only submitted to second-order quadrupole interactions [29].

3.4. Isotropic spectral width and minimum evolution time

Because only second-order dephasings (ϕ_{Q2}) are refocused by the STMAS sequence, it is mandatory in all STMAS-based experiment to rotor-synchronize the evolution time. In MQMAS it is highly recommended to do the same for three reasons: (i) a small number of t_1 steps are then used, thereby minimizing the acquisition time, (ii) all sidebands are aliased onto the center band, thus maximizing the S/N ratio and simplifying the interpretation of the spectra, and (iii) distortions with respect to MAS spectra are minimized [30]. However, under rotor synchronization, and for identical spinning speed, the isotropic sheared spectral-width (in ppm) Fig. 8, so that the minimum number of t_1 steps required to not truncate the signal, are doubled in STMAS-based experiments with respect to 3QMAS [5]. Thus, using half the spinning speed in DQF–STMAS experiments provides the same isotropic spectral width (in ppm) as with 3QMAS with the same required minimum number of t_1 steps. This argument for the spinning speed becomes a very large advantage for DQF–STMAS when applied to experiments performed at very large magnetic fields. Indeed, in all 2D rotor synchronized experiments, the minimum rotor speed necessary to observe on one particular sample the full frequency range in the indirect spectral-width is proportional to the static magnetic field. This means that STMAS experiments are well adapted to very high-field spectrometers, as they require only half the spinning speed required by rotor-synchronized 3QMAS experiment. In the latter case and especially with very high-field spectrometers, this minimum speed may sometimes be impossible to access, even with very small rotor diameters and hence very small sample volume, in case of nuclei presenting large chemical shift ranges.

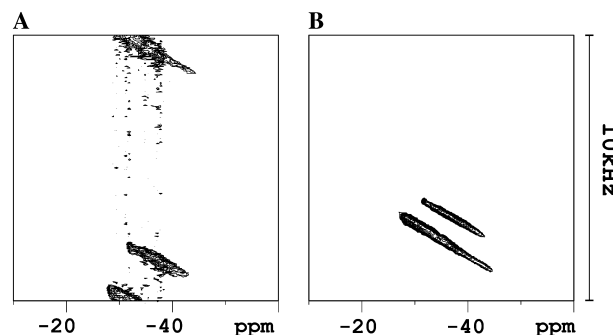In any case, it is well-known that the MQMAS sensitivity decreases with increasing speed, especially for

Fig. 8. $S = 3/2$: ^{87}Rb rotor-synchronized 2D spectra of RbNO$_3$ described using the same unified ppm scaling. Hyper-complex z-filter (A) 3QMAS, (B) DQF–STMAS. Echo/anti-echo and SPAM$_{E/AE}$ DQF–STMAS spectra are identical to (B). $v_0 = 130.9$ MHz, $v_R = 10$ kHz. The isotropic spectral width in (A) is half that in (B), thus leading to a folding of one of the resonances.

$S = 3/2$ in case of weak RF-field for hard-pulses [31]. This is not at all the case in DQF–STMAS (Fig. 7B), where oppositely it slightly increases due to the fact that the first FID, which is attenuated by ϕ_{Q2} dephasings and T'_2 losses, is recorded for smaller evolution time ($t_1 = 1/v_R$).

In the case of nuclei submitted to small or moderate quadrupole interaction and large CSA (e.g., ^{51}V), a very fast spinning speed is often preferred to decrease the number of ST sidebands along δ_2. All previous phenomenon (small C_Q, large CSA, fast spinning speed) then combine to decrease the sensitivity in 3QMAS. This is not the case in STMAS where the sensitivity is less dependent on the CSA (Fig. 7A) and the spinning speed (Fig. 7B), and remains reasonable for small C_Q values (Fig. 5). The sensitivity gain with respect to 3QMAS may then be much larger than the factor of 2–3 that was described in Fig. 6.

4. SPAM DQF–STMAS

4.1. Principle

Very recently, it has been shown that using after HP_2 all quantum levels instead of a single one allows doubling the echo and anti-echo signals in MQMAS [14,15]. This concept has been referred to as soft-pulse added mixing (SPAM). In SPAM-based experiments, phases related to HP_2 and the following soft-pulse must be fixed to $\pm x$ to alias signals related to all coherence levels in between these two pulses. They have same or opposite signs according to whether the global transfer for these two pulses is in between quantum levels of opposite or identical signs, respectively. This is completely opposite to original MQMAS or STMAS experiments, for which all phases must be cycled to select only one quantum level in between the two pulses. When using SPAM, phases of other pulses, and that of the receiver, are calculated by assuming a $0Q$ level between HP_2 and the following SP. The delay in between these two pulses must be as short as possible to avoid dephasings for magnetizations not located on zero quantum level. Quantum levels used during t_1 for the anti-echo pathway are symmetrical with those used for the echo pathway, which implies a change of sign for the phase of the soft-pulse following HP_2. It is therefore impossible to record simultaneously the echo and anti-echo pathways in SPAM-based experiments.

4.2. Optimization of echo and anti-echo pathways

We first analyzed the optimization of echo and anti-echo signals observed when using SPAM into DQF–STMAS method. Experimentally, we have recorded

the FID observed for the first $t_1 = T_R$ step, and used the following coherence transfer pathways corresponding to the SPAM echo signal:

$$SPAM_E \ 0Q \rightarrow -1Q(T_R - t_\pi) \rightarrow -2Q(t_\pi) \rightarrow all \rightarrow -1Q(t_2)$$
$$\text{if } S = 3/2, \tag{6}$$

$$SPAM_E \ 0Q \rightarrow +1Q(T_R - t_\pi) \rightarrow +2Q(t_\pi) \rightarrow all \rightarrow -1Q(t_2)$$
$$\text{if } S > 3/2. \tag{7}$$

For the theoretical optimization, we have calculated the powder averaged final CT coherence observed with these transfer pathways for $t_1 = T_R$ and $t_2 = R(S)T_R$. For the SPAM anti-echo ($SPAM_{AE}$) signal, quantum levels in between HP_1 and HP_2 have been changed in sign with respect to Eq. (6,7). We have verified experimentally (Fig. 9) and theoretically, (i) that optimized values for HP_1 are always identical in all STMAS-based experiments, (ii) that with SPAM, HP_2 lengths are always optimal when the $\pm 2Q \rightarrow 0Q$ transfer is maximal and thus, are identical to their optimal values in z-filter experiment, and (iii) that optimal values of the soft-pulse just following HP_2 are always close to 90_s°, but that this value is not critical (Fig. 9).

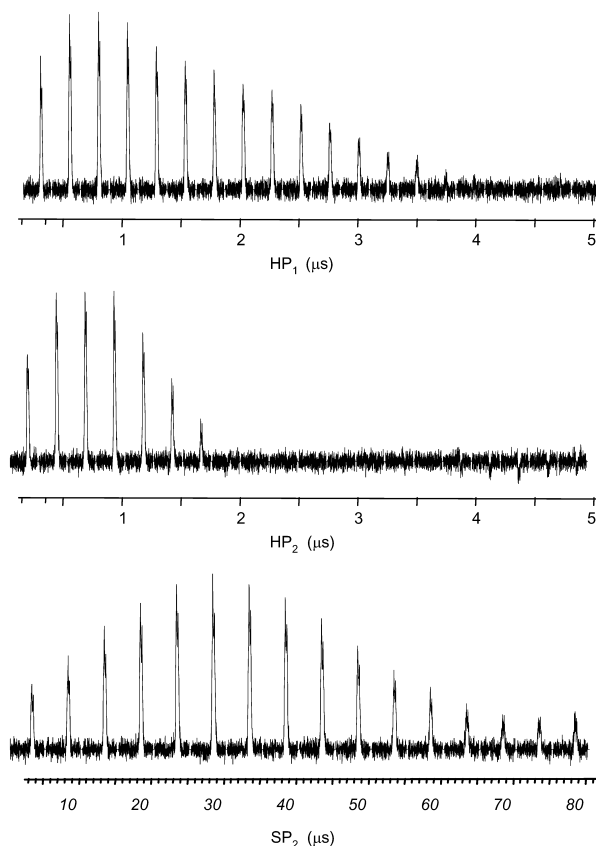Fig. 9. $S = 5/2$: optimization of the ^{27}Al SPAM echo signal of AlPO$_4$ berlinite: $\{0Q \rightarrow 1Q \ (T_R - t_\pi) \rightarrow 2Q \ (t_\pi) \rightarrow all \rightarrow -1Q \ (t_2)\}$ versus pulse-lengths: HP_1, HP_2, SP_2. RF-field amplitudes were: 108 kHz and 3300 Hz for hard-pulses and soft-pulses, respectively.

In a second step, for $S = 5/2$ (^{27}Al), we have measured as a function of the second soft-pulse length (SP$_2$), the contribution on the final signal that can be obtained from each quantum level involved in between HP$_2$ and SP (Fig. 10A). For the optimum pulse length (30 μs) for the total SPAM$_E$ signal, which corresponds to 107°_s (RF = 3300 Hz), we have also represented the three contributions arising through $+1Q$, $0Q$, and $-1Q$ levels observed when using either the echo (Fig. 10B) or the anti-echo (Fig. 10C) pathway. It can be verified that the sum of these three signals is always equal (within a few percents) to the total SPAM signal observed by aliasing signals coming from all quantum levels. This means that transfers of signals not located on $0Q$ or $\pm 1Q$ levels after HP$_2$ are negligible due to SP weak RF-field. Moreover, contributions from these three pathways are proportional to 0.5, 0.4, and 0.1 (echo), and 0.2, 0.5, and 0.3 (anti-echo) for $+1Q$, $0Q$, and $-1Q$ levels, respectively. Including SPAM into the pulse sequence more than doubles the echo and anti-echo signals as compared to that obtained with the z-filter experiment. However, it must be noted that for identical experimental specifications (RF-fields and spinning speed), the total intensities observed with anti-echo pathway is approximately 36% smaller than with echo pathway (compare Figs. 10B and C).

SPAM concept may also be incorporated in the full-echo (SPAM$_{FE}$) or full-antiecho (SPAM$_{FAE}$) acquisition schemes [12], which are depicted in Fig. 1F along with the coherence orders selected (Fig. 1G):

$$\text{SPAM}_{FAE} : 0Q \to 1Q(t_1 - t_\pi) \to 2Q(t_\pi) \to \text{ all}$$
$$\to 1Q(\tau + Rt_1) \to -1Q(\tau + t_2) \quad \text{if } S = 3/2,$$
(8)

$$\text{SPAM}_{FE} : 0Q \to 1Q(t_1 - t_\pi) \to 2Q(t_\pi) \to \text{ all } \to 1Q(\tau)$$
$$\to -1Q(\tau + Rt_1 + t_2) \quad \text{if } S > 3/2.$$
(9)

We have seen previously that the original (without SPAM) DQF–STMAS versions of full-echo or full-antiecho experiments were approximately twice as efficient as the z-filter versions (Fig. 5). However, the gain obtained with SPAM for full-echo and full-antiecho sequences is less than previously (ca. 2). This decrease of the SPAM gain is related to the use of an additional soft-pulse ($\approx 90^\circ_s$), which implies that the $2Q \to 1Q$ transfer is performed indirectly in SPAM (through the $0, \pm 1Q$ levels), whereas it is performed directly in the full-echo or full-antiecho acquisition performed without SPAM (compare Figs. 1D–G). Globally, the efficiency obtained with these SPAM$_{FE}$ or SPAM$_{FAE}$ pathways (Eq. (8) and (9)) is only 1.4 larger (Fig. 11) than that obtained with SPAM$_E$ pathways (Eq. (6) and (7)). By taking into account the supplementary attenuation factor of SPAM$_{FE}$ and SPAM$_{FAE}$: $\exp(-\tau/T'_{2ST} - \tau/T'_{2CT})$, the maximum signal may thus often be observed using the SPAM$_E$ pathway.

4.3. Intensities of 2D spectra

In z-filter experiments both echo and anti-echo pathways are collected simultaneously leading to a single amplitude-modulated signal with respect to t_1. This
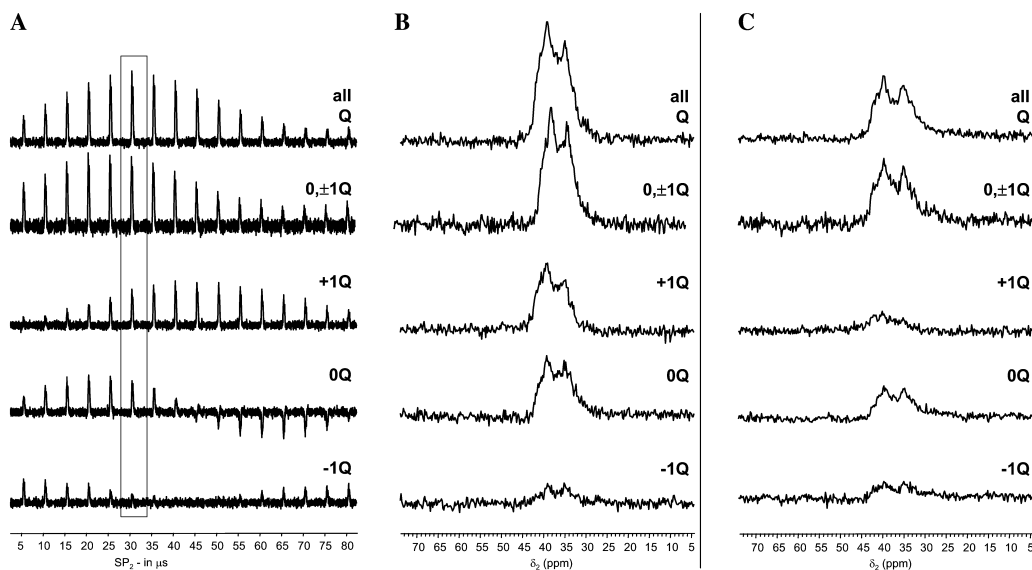

Fig. 10. $S = 5/2$: ^{27}Al SPAM signals of AlPO$_4$ berlinite. (A) Echo signals versus SP$_2$. (B) Echo and (C) anti-echo spectra, for the echo-optimum SP$_2$ = 30 μs pulse length. In the three figures (A–C), individual contributions of signals passing after HP$_2$ through the $-1Q$, $0Q$, and $+1Q$ levels are shown, so that their sum and the total SPAM signal. $v_0 = 130.9$ MHz, $v_R = 10$ kHz, RF-field amplitudes were: 108 kHz and 3300 Hz for hard-pulses and soft-pulses, respectively. The two groups of selected spectra (B and C) are taken under "echo-SPAM optimal conditions". This leads to reduced (35%) anti-echo signal amplitudes. To balance the echo/anti-echo pathways, a slightly reduced value of SP$_2$ = 25 μs should have to be used.
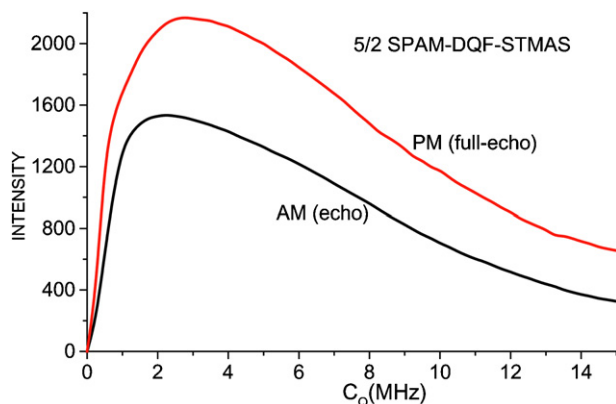
Fig. 11. $S = 5/2$: SPAM DQF–STMAS efficiency of the echo ($0 \rightarrow 1 \rightarrow 2 \rightarrow$ all $\rightarrow -1$) and full-echo ($0 \rightarrow 1 \rightarrow 2 \rightarrow$ all $\rightarrow 1 \rightarrow -1$) pathways as a function of C_Q(0–15 MHz), with RF (HP) = 150 kHz. All other specifications as in Fig. 5.

Fig. 12. $S = 3/2$: isotropic projection (with unified ppm scaling [5]) of ^{87}Rb 2D sheared spectra of RbNO$_3$. Hyper-complex z-filter spectra: 3QMAS (A) and DQF–STMAS (B). DQF–STMAS spectra: echo/anti-echo (C) and SPAM$_{E/AE}$ (D). $v_0 = 130.9$ MHz, $v_R = 10$ kHz. The t_1 noise can easily be observed in spectra (B–D).

leads to a frequency sign indiscrimination of the resonances with respect to the carrier frequency along the δ_1 dimension. This problem is solved by using the hyper-complex [32] or TPPI [33] acquisition and data treatment.

On the contrary, when using echo and anti-echo signals, the SPAM concept requires observing two separated phase-modulated signals, one for the echo and one for the anti-echo pathways. This leads to the echo/anti-echo method and data treatment (SPAM$_{E/AE}$) in which the real part of the final spectrum, is in pure absorption mode [34]. As the data from which the final spectrum is computed are phase-modulated with respect to t_1, frequency discrimination and phase corrections are achieved in the δ_1 dimension.

In liquids, the echo and anti-echo lead to almost symmetrical amplitudes, which is not the case in STMAS. Due to this asymmetry, the anti-echo amplitude decreases much faster than the echo. Consequently the signal is mainly related to the echo pathway and the number of indirect steps can be largely reduced in echo/anti-echo experiments by collecting fewer anti-echoes. One must also be reminded that in order to achieve the same resolution in δ_1, hyper-complex method records each t_1 increment twice, one with sine and one with cosine modulation [32]. TPPI and echo–antiecho double the number of scans for each t_1 steps with respect to other methods [35]. Therefore, the total number of indirect steps is the same for all experiments (hyper-complex, TPPI, echo/anti-echo) with same δ_1 resolution [35].

In Fig. 12, we have represented the isotropic projections that can be obtained on ^{87}Rb ($S = 3/2$) 2D spectra of a well-crystallized test compound: RbNO$_3$, which presents three different ^{87}Rb species all resolved in the 2D spectra: $C_Q = 1.79$, 1.75, 1.99 MHz; $\eta_Q = .55$, .18, .91; $\delta_{CS} = -31.3$, -26.6, -28.5 ppm [36]. The
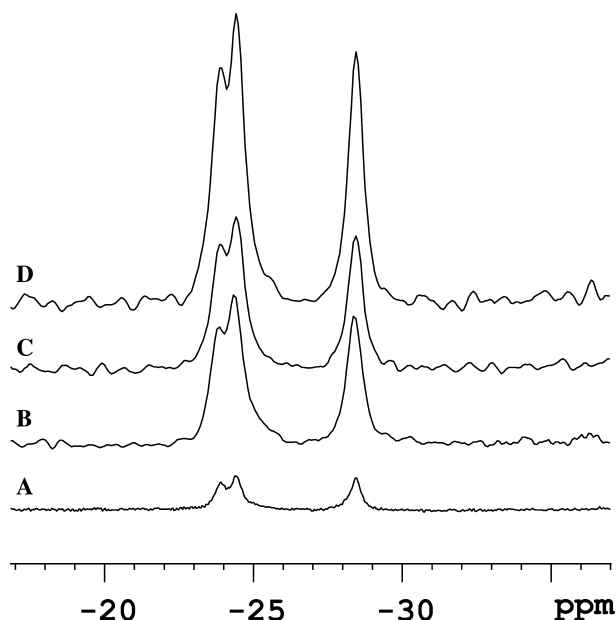
experiments were carried out on a Bruker Avance 400 MHz spectrometer at 9.4 T ($v_0 = 130.87$ MHz) with RF-field amplitudes of 120 and 5 kHz for hard- and soft-pulses, respectively. Fig. 12A is the result from a z-filter 3QMAS experiment, Fig. 12B is the result from a z-filter DQF–STMAS experiment, Fig. 12C is the result from an echo/anti-echo DQF–STMAS acquisition, and Fig. 12D is the result from SPAM$_{E/AE}$ DQF–STMAS sequence of Fig. 1A and C. All experiments were rotor-synchronized during t_1 ($v_R = 10$ kHz) and took the same amount of time. The very large sensitivity gain, with respect to MQMAS experiments, that is often encountered in all STMAS-type experiments is easily observable by comparing spectra displayed in Figs. 12A and B. In the case of rubidium sulfate, it has even been reported a sensitivity gain as large as 9.2 [22]. In addition to this very large sensitivity another specification can be observed in all STMAS-based spectra (Figs. 12B–D): the large increase of the noise level with respect to MQMAS experiments (Fig. 12A). This "t_1 noise," which comes from the small spinning speed fluctuations (1–2 Hz) (Fig. 4A), is only visible on the isotropic projections (δ_{iso}) and not onto the anisotropic MAS projections (δ_2) [13]. By comparing Figs. 12B and C, it can be observed that both methods (hyper-complex and echo/anti-echo) give the same sensitivity, but that the latter one increases the noise level by a factor $\sqrt{2}$. This is due to the fact that the echo and anti-echo signals must then be acquired separately in echo/anti-echo method instead of simultaneously in z-filter experiment. The

low noise level as well as the robustness of the experiment are the two main reasons that explain why the z-filter approach is at the moment the most frequently used MQMAS method. It must be noted that, in spite of the fact echo and anti-echo sensitivities are slightly different in SPAM (Fig. 10), dispersive parts are invisible on the 2D SPAM spectra (Fig. 8). There are two ways to decrease these dispersive parts, either by using two different SP_2 lengths for the echo and anti-echo acquisitions, or by slightly scaling the anti-echo FIDs. Indeed, in Fig. 10, the echo-optimum SP_2 lengths (30 μs) has also been used for anti-echo acquisition. When the anti-echo optimum SP_2 length (25 μs) is used for the anti-echo acquisition, the balance is much better. Of course, this requires optimizing one additional SP_2 pulse-length. In the case of perfectly crystallized compounds with close resonances, this may not still be sufficient for resolution purpose, and an a posteriori scaling of the anti-echo FIDs may also have to be used. This very small scaling, which only changes the dispersive signal and not the absorption part, does not change the S/N ratio as only very few anti-echo t_1 steps are not zero-filled. By comparing Fig. 12B–D, the signal enhancement obtained in DQF–STMAS experiments with $SPAM_{E/AE}$ over the z-filter and echo/anti-echo methods is by a factor of 2. However, for the same experimental time, the signal can still be increased by recording only a few FIDs for the anti-echo pathway and zero-filling all other FIDs to decrease the noise. Indeed, due to the negative, $-R(S)$, slope of the anti-echo signal in the time domain, the contribution of the anti-echo pathway to the signal becomes negligible, if not non-existent, after a few t_1 steps, particularly for samples having short homogeneous T_2' time constants or submitted to large quadrupole interactions and/or distribution of surroundings. Therefore, long t_1 steps

correspond to longer experimental times and to an increase in noise only. The signal is then proportional to the number of scans accumulated for each t_1 increment. Since the experimental time and hence the total number of scans are the same, the noise level remains identical in all echo/anti-echo spectra, whatever the number of recorded anti-echo t_1 slices be. An easy way to even double the signal and the S/N ratio with respect to Fig. 12D ($SPAM_{E/AE}$) is to avoid recording any anti-echo FID, and to zero-fill them. With respect to Fig. 12D, we gain an additional factor of two for the signal (not shown), which then becomes 18 times larger than with the z-filter 3QMAS experiment. However, this additional doubling of the S/N ratio is obtained at the expense of a small amount of additional dispersive signal. It must be kept in mind that even with the z-filter experiment, a dispersive signal is often observed, especially in case of sample with multiple sites with large differences in the quadrupolar strengths. Its amount increases with the second-order quadrupole interaction, with off-resonance irradiation, and also with decreasing RF-field. Dispersive signals are invisible on the projections, because their intensities integrated over F_1 or F_2 are null. However, they may limit the resolution of 2D spectra for well-crystallized compounds with narrow and close resonances. A complete description of the experimental setting up of STMAS-based experiments has already been done extensively several times (e.g. [13,18,21]). In the caption of Fig. 13, the phase-cycling for the $SPAM_{E/AE}$ DQF–STMAS experiment is provided. However, the most-important part of the $SPAM_{E/AE}$ MQMAS [15] and $SPAM_{E/AE}$ DQF–STMAS experiments remains the software required to acquire and process the data, so that to perform the shearing process and introduce the unified ppm scaling [5]. This software will be soon available on the Bruker web site.
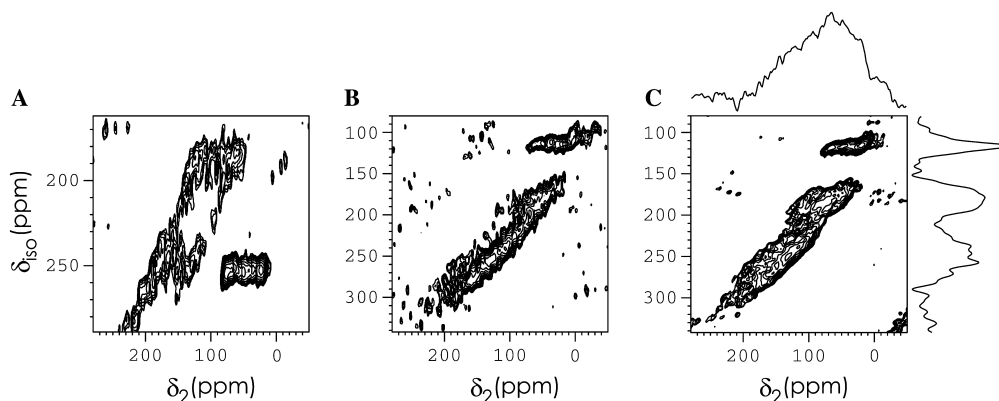

Fig. 13. $S = 5/2$: ^{17}O sheared 2D spectra of $Nb_{1.91}P_{2.82}O_{12}$. (A) $SPAM_{E/AE}$ 3QMAS recorded in 64 h, without any anti-echo t_1 slice. (B) Hypercomplex z-filter DQF–STMAS recorded in 17 h. (C) $SPAM_{E/AE}$ DQF–STMAS recorded in 17 h without any anti-echo t_1 slice. $\nu_0 = 54.2$ MHz, $\nu_R = 12$ kHz. The isotropic spectral width in (A) is half that in (B and C), thus leading to a folding of one of the resonances. In ^{27}Al $SPAM_{E/AE}$ DQF–STMAS, we have used the following phase cycling: $HP_1 = x, y, -x, -y$; $SP_1 = x * 4, y * 4, -x * 4, -y * 4$; $HP_2 = 0$; $SP_2 = x$ (E) or $-x$ (AE); receiver phase: $E = -HP_1 - SP_1 + 2HP_2 + SP_2 = -HP_1 - SP_1$, $AE = HP_1 + SP_1 - 2HP_2 + SP_2 = HP_1 + SP_1 + SP_2$.

4.4. Utilization on distributed samples

In the previous sections, we have demonstrated theoretically and experimentally on well-crystalline test samples, the advantages of using $SPAM_{E/AE}$ with the DQF–STMAS method, especially in its truncated version. To demonstrate practically this advantage, we have used the $SPAM_{E/AE}$ method to record ^{17}O DQF–STMAS spectra on an ^{17}O-enriched distributed powder sample of formula $Nb_{1.91}P_{2.82}O_{12}$. This material crystallizes in the orthorhombic system, with *Pbcn* space group, and at room temperature its lattice parameters are as follows: $a = 12.0819$ Å [37], $b = 8.6848$ [37], $c = 8.7452$ [38]. The basis structure consists of a 3D framework of the $Sc_2(WO_4)_3$ type, with sharing corners NbO_6 octahedra and PO_4 tetrahedra, leading theoretically to the formula $Nb_2P_3O_{12}$. When perfectly crystallized without any vacancies, this sample presents six different oxygen sites, two different phosphorus sites and a single niobium site (with oxidation number of 5). However, due to our preparation method, the actual formula of the sample we have used is slightly different consequently to both Nb and P vacancies. Zah-Letho et al. [37,38] have showed that the occupancies of Nb and P are then respectively equal to 95.5 and 94%, leading to the formula $Nb_{1.91}P_{2.82}O_{12}$ [38]. The presence of these vacancies implies a large distribution of surroundings in our sample.

This compound was synthesized starting from the commercial products $(NH_4)_2HPO_4$ and Nb_2O_5, which were mixed and finely crushed. The mixture was heated in a platinum crucible, in air, up to 360 °C, and hold at this temperature for 30 h. The heating rate must be at least 2 K/min, to prevent the formation of significant amounts of $Nb_3(NbO)_2(PO_4)_7$ [37]. After cooling, the product was washed repeatedly with water, ethanol, ether, and acetone in turn, to remove the excess phosphorus oxide, and then dried in an oven at 100 °C before final heating at 400 °C for 15 h. The product is a white, finely divided, crystalline powder [38]. For the preparation of our sample for NMR experiments, the $Nb_{1.91}P_{2.82}O_{12}$ material was ^{17}O-enriched in an oven (constant humidity rate), starting from water ^{17}O-enriched. We estimate the ^{17}O enrichment level to be inferior to 30%.

We will now use this sample to show the interest of using SPAM methods for samples presenting a very weak NMR signal. Fig. 13 shows three ^{17}O 2D spectra recorded on this compound: hyper-complex *z*-filter DQF–STMAS (B), and only echo $SPAM_{E/AE}$ (with zero-filled anti-echo FIDs) 3QMAS (A) or DQF–STMAS (C). We used a Bruker Avance-400 spectrometer, the Larmor frequency was $v_0 = 54.2$ MHz, the spinning speed $v_R = 12$ kHz, and the RF-field approximately 100 and 5 kHz for the hard- and soft-pulses, respectively. We tried unsuccessfully to record a *z*-filter 3QMAS spectrum on this compound; after several days

we observed only noise. We were then able to obtain a decent 3QMAS spectrum in 64 h by using the SPAM concept (Fig. 13A). However it must be noted that due to insufficient spinning speed, the isotropic spectral width was too much limited and the narrow resonance observed at $\delta_2 = 50$ ppm was folded at $\delta_{iso} = 250$ ppm. We then recorded a spectrum with hyper-complex *z*-filter DQF–STMAS (Fig. 13B). The S/N ratio was worse than previously, but the spectra was acquired in 17 h instead of 64 h. It is very important to note that the isotropic spectral width is doubled in DQF–STMAS and hence is then quite sufficient for frequency spread along δ_{iso}. This problem of insufficient spinning speed should still be more critical by recording the 2D spectra at higher magnetic fields. When using the SPAM concept, the S/N ratio became very good, even with only 17 h of accumulation (Fig. 13C). As can be observed by comparing the three spectra, even without recording any t_1 slice, the dispersive parts are nearly undetectable on the $SPAM_{E/AE}$ spectra, due to the broadness of the resonance. Thus, by using simultaneously the DQF–STMAS method and the SPAM concept, spectra that are completely invisible with the *z*-filter 3QMAS spectra become easily observable. It must noted that there is no "t_1 noise" observed in Figs. 13B and C. This is due to the fact that this "t_1 noise" is proportional to the signal, which is weak in this case. Contrary to what is observed in Fig. 12, it is therefore embedded in the thermal noise.

5. Conclusion

The DQF–STMAS method is a very promising method. Contrary to previous STMAS methods, it allows a much simpler optimization of all experimental parameters, directly on the FIDs. With respect to MQMAS, this method presents the great advantage of a much larger sensitivity, which is moreover less dependent on the spinning speed and on CSA. In addition, to cover the full isotropic spectral width, the method needs only half the spinning speed required by 3QMAS, which is another great advantage especially at very high-magnetic fields. There are however two technical limitations related to all STMAS-based methods: they require a perfect adjustment of the magic angle and a perfectly stable spinning speed. Independently of their respective technical advantages and limitations, the two methods are in fact complementary as their comparison allows deducing species that are submitted to motions or that are close to mobile nuclei (e.g., water molecules) [29].

The SPAM principle (adding constructively several pathways instead of using a single one), is a simple but efficient idea. It can be used with echo/anti-echo ($SPAM_{E/AE}$), or full-echo ($SPAM_{FE}$ if $S > 3/2$), or full anti-echo ($SPAM_{FAE}$ if $S = 3/2$) methods. However, by taking into account the fact that there is an addition-

al loss factor $(\exp(-\tau/T'_{2ST} - \tau/T'_{2CT}))$ for the $SPAM_{FE}$ and $SPAM_{FAE}$ experiments, and also the fact that an additional S/N gain close to 2 can be obtained with $SPAM_{E/AE}$ experiments recorded with few anti-echo t_1 slices, $SPAM_{E/AE}$ may often be more efficient than $SPAM_{FE}$ or $SPAM_{FAE}$ experiments. $SPAM_{E/AE}$ largely increases the S/N ratio of DQF–STMAS experiments, especially in the case of distributed samples where no or very few anti-echo t_1 slices are necessary. It presents the great advantage of being robust and being for the users completely identical to the previous z-filter DQF–STMAS method (two hard-pulses and two (π_s and $\pi_s/2$) soft-pulses) as only the phase cycling differs. This means that its experimental optimization is very simple and only concerns the two hard-pulse lengths (their RF-amplitude being set at its maximum), and thus can be used on samples with a low sensitivity (e.g., low gamma nuclei). The main advantage of the $SPAM_{E/AE}$ method, over z-filter, results partly from the fact that only few anti-echo t_1 steps need to be recorded without affecting the broad 2D resonance line shapes in distributed samples. As an example, on glasses it has been our experience that no, or less than five, anti-echo t_1 slices are necessary to obtain 2D $SPAM_{E/AE}$ spectra without any detectable dispersive signals. The SPAM principle can be combined with other solid-state NMR tools for further S/N enhancement, such as initial pre-saturation [39,40] and a posteriori echo CPMG recycling [41]. Indeed, the latter tool leads to a large S/N gain when homogeneous transverse relaxation is much smaller than the inhomogeneous one [42].

After, this article was sent for publication, we have been aware of a new method concerning SPAM-MQMAS [43], which may a priori also be used for SPAM-STMAS. Similarly to the way proposed by Gan and Kwak [14], this article combines for MQMAS the multiplex phase cycling method [44], with the SPAM concept. The main difference between the two proposals is that the multiplex approach is introduced either only after the second hard-pulse [14], or also before this pulse [43]. In both cases, S/N gains with respect to z-filter are similar (ca. 1.7 for 3QMAS) but smaller than with SPAM-3QMAS (ca. 3) [15], however dispersive parts are then perfectly cancelled. According to the fact that the main purpose is to increase either the resolution, or the S/N ratio, multiplex hyper-complex [14,43] or echo/anti-echo [15] SPAM methods should hence be used.

References

[1] E.R. Andrew, A. Bradbury, R.G. Eades, Nature (London) 182 (1958) 1659.

[2] L. Frydman, J.S. Harwood, Isotropic spectra of half-integer quadrupolar spins from bidimensional magic-angle-spinning NMR, J. Am. Chem. Soc. 117 (1995) 5367–5368.

[3] Z.H. Gan, Isotropic NMR spectra of half-integer quadrupolar nuclei using satellite transitions and magic-angle-spinning, J. Am. Chem. Soc. 122 (2000) 3242–3243.

[4] J.P. Amoureux, C. Fernandez, Triple, quintuple and higher-order multiple quantum MAS NMR of quadrupolar nuclei, Solid State NMR 2 (1998) 83–88;
, Solid State NMR 16 (2000) 339–343.

[5] J.P. Amoureux, C. Huguenard, F. Engelke, F. Taulelle, Unified representation of MQMAS and STMAS NMR of half-integer quadrupolar nuclei, Chem. Phys. Lett. 356 (2002) 497–504.

[6] A. Medek, J.S. Harwood, L. Frydman, Multiple-quantum magic-angle spinning NMR: a new method for the study of quadrupolar nuclei in solids, J. Am. Chem. Soc. 117 (1995) 12779–12787.

[7] G. Wu, D. Rovnyak, B. Sun, R.G. Griffin, High-resolution multiple-quantum MAS NMR spectroscopy of half-integer quadrupolar nuclei, Chem. Phys. Lett. 249 (1996) 210–217.

[8] J.P. Amoureux, C. Fernandez, L. Frydman, Optimized multiple-quantum magic-angle spinning NMR experiments on half-integer quadrupoles, Chem. Phys. Lett. 295 (1996) 347–355.

[9] J.P. Amoureux, C. Fernandez, S. Steuernagel, Z-filtering in MQMAS NMR, J. Magn. Reson. A 123 (1996) 116–118.

[10] D. Massiot, B. Touzo, D. Trumeau, J.P. Coutures, J. Virlet, P. Florian, P.J. Grandinetti, Two-dimensional magic-angle spinning isotropic reconstruction sequences for quadrupolar nuclei, Solid State NMR 6 (1996) 73–83.

[11] S.P. Brown, S. Wimperis, Two-dimensional multiple-quantum MAS NMR of quadrupolar nuclei, acquisition of the whole echo, J. Magn. Reson. 124 (1997) 279–285.

[12] K.J. Pike, S.E. Ashbrook, S. Wimperis, Two-dimensional satellite transition MAS NMR of quadrupolar nuclei: shifted echoes, high-spin nuclei and resolution, Chem. Phys. Lett 345 (2001) 400–408.

[13] S.E. Ashbrook, S. Wimperis, Satellite-transition MAS NMR of spin $I = 3/2, 5/2, 7/2$, and $9/2$ nuclei: sensitivity, resolution, and practical implementation, J. Magn. Reson. 156 (2002) 269–281.

[14] Z. Gan, H.T. Kwak, Enhancing MQMAS sensitivity using signals from multiple coherence transfer pathways, J. Magn. Reson. 168 (2004) 346–351.

[15] J.P. Amoureux, L. Delevoye, S. Steuernagel, Z. Gan, S. Ganapathy, L. Montagne, Increasing the sensitivity of 2D high-resolution NMR methods applied to quadrupolar nuclei, J. Magn. Reson. 172 (2005) 268–278.

[16] R.R. Ernst, G. Bodenhausen, A. Wokaun, Principles of Nuclear Magnetic Resonance in One and Two Dimensions, Clarendon, Oxford, 1987.

[17] Z. Gan, Satellite transition magic-angle spinning nuclear magnetic resonance spectroscopy of half-integer quadrupolar nuclei, J. Chem. Phys. 114 (24) (2001) 10845–10853.

[18] C. Huguenard, F. Taulelle, Z. Gan, Optimizing STMAS, J. Magn. Reson. 156 (2002) 131–137.

[19] H.T. Kwak, Z. Gan, Double-quantum filtered STMAS, J. Magn. Reson. 164 (2003) 369–372.

[20] G. Mali, G. Fink, F. Taulelle, Double-quantum homonuclear correlation magic-angle spinning nuclear magnetic resonance

spectroscopy of dipolar-coupled quadrupolar nuclei, J. Chem. Phys. 120 (2004) 2835–2845.

[21] S.E. Ashbrook, S. Wimperis, High-resolution NMR of quadrupolar nuclei in solids: the satellite-transition magic angle spinning (STMAS) experiment, Prog. NMR. Spectrosc. 45 (2004) 53–108.

[22] S.E. Ashbrook, S. Wimperis, SCAM-STMAS: satellite-transition MAS NMR of quadrupolar nuclei with self-compensation for magic-angle misset, J. Magn. Reson. 162 (2003) 402–416.

[23] T. Giavani, H. Bildsoe, J. Skibsted, H.J. Jakobsen, ^{14}N MAS NMR spectroscopy and quadrupole coupling data in the characterization of the IV-III phase transition in ammonium nitrate, J. Phys. Chem. B 106 (2002) 3026–3032.

[24] E. Hughes, T. Gullion, A simple, inexpensive, and precise magic angle spinning speed controller, Solid State NMR 26 (2004) 16–21.

[25] N.G. Dowell, S.E. Ashbrook, S. Wimperis, Satellite-transition MAS NMR of low-γ nuclei at natural abundance: sensitivity, practical implementation, and application to ^{39}K ($I = 3/2$) and ^{25}Mg ($I = 5/2$), J. Phys. Chem. B 108 (2004) 13292–13299.

[26] L. Marinelli, A. Medek, L. Frydman, Composite-pulse excitation schemes for MQMAS NMR of half-integer quadrupolar spins, J. Magn. Reson. 132 (1998) 88–95.

[27] Z. Gan, P. Srinivasan, J.R. Quine, S. Steuernagel, B. Knott, Third-order effect in solid-state NMR of quadrupolar nuclei, Chem. Phys. Lett. 367 (2003) 163–169.

[28] S. Wi, S.E. Ashbrook, S. Wimperis, L. Frydman, Second-order quadrupole-shielding effects in magic-angle spinning solid-state nuclear magnetic resonance, J. Chem. Phys. 11 (7) (2003) 3131–3140.

[29] S.E. Ashbrook, S. Antonijevic, A.J. Berry, S. Wimperis, Motional broadening: an important distinction between multiple-quantum and satellite-transition MAS NMR of quadrupolar nuclei, Chem. Phys. Lett. 364 (2002) 634–642.

[30] D. Massiot, Sensitivity and lineshape improvements of MQMAS by rotor-synchronization, J. Magn. Reson. A 122 (1996) 240–244.

[31] J.P. Amoureux, M. Pruski, D.P. Lang, C. Fernandez, The effect of rf-power and spinning speed on MQMAS NMR, J. Magn. Reson. 131 (1998) 170–175.

[32] D.J. States, R.A. Haberkorn, D.J. Ruben, J. Magn. Reson. 48 (1982) 256.

[33] A. Bax, R. Freeman, S.P. Kempsell, J. Magn. Reson. 41 (1980) 349.

[34] A.L. Davis, J. Keeler, E.D. Laue, D. Moskau, Experiments for recording pure-absorption heteronuclear correlation spectra using pulse field gradients, J. Magn. Reson. 98 (1992) 207–216.

[35] D. Marion, K. Wüthrich, Biochem. Biophys. Res. Com. 113 (1983) 967.

[36] J.H. Baltisberger, S.L. Gam, E.W. Wooten, T.H. Chang, K.T. Mueller, A. Pines, ^{87}Rb dynamic-angle spinning NMR of inorganic rubidium salts, J. Am. Chem. Soc. 114 (1992) 1489–1493.

[37] J.J. Zah-Letho, A. Jouanneaux, A.N. Fitch, A. Verbaere, Y. Piffard, M. Tournoux, Eur. J. Solid State Inorg. Chem. 29 (1992) 1309.

[38] J.J. Zah-Letho, A. Verbaere, A. Jouanneaux, F. Taulelle, Y. Piffard, M. Tournoux, J. Solid State Chem. 116 (1995) 335–342.

[39] P.K. Madhu, A. Golbourt, L. Frydman, S. Vega, Sensitivity enhancement of the MQMAS NMR experiment by fast amplitude modulation of the pulses, Chem. Phys. Lett. 307 (1999) 41–47.

[40] Z. Yao, H.T. Kwak, D. Sakellariou, L. Emsley, P.J. Grandinetti, Sensitivity enhancement of the central transition of quadrupolar nuclei under MAS, Chem. Phys. Lett. 327 (2000) 85–90.

[41] T. Vosegaard, F.H. Larsen, H.J. Jakobsen, P.D. Ellis, N.C. Nielsen, Sensitivity-enhanced multiple-quantum MAS NMR of half-integer quadrupolar nuclei, J. Am. Chem. Soc. 119 (1997) 9055–9056.

[42] R. Lefort, J.W. Wiench, M. Pruski, J.P. Amoureux, Optimization of data acquisition and processing in Carr–Purcell–Meiboom–Gill multiple-quantum MAS NMR, J. Chem. Phys. 116-6 (2002) 2493–2501.

[43] N. Malicki, L. Mafra, A.A. Quoineaud, J. Rocha, F. Thibault-Starzyk, C. Fernandez, Multiplex MQMAS NMR of quadrupolar nuclei, Solid State NMR 28 (2005) 13–21.

[44] N. Ivchenko, C.E. Hughes, M.H. Levitt, Multiplex phase cycling, J. Magn. Reson. 160 (2003) 52–58.